Enormous nuclear surface diffuseness of Ne and Mg isotopes in the island of inversion

V. Choudhary [1,*] W. Horiuchi [2,†] M. Kimura,[2,3,4,‡] and R. Chatterjee[1,§]
[1]*Department of Physics, Indian Institute of Technology Roorkee, Roorkee 247 667, India*
[2]*Department of Physics, Hokkaido University, 060-0810 Sapporo, Japan*
[3]*Nuclear Reaction Data Centre, Faculty of Science, Hokkaido University, 060-0810 Sapporo, Japan*
[4]*RIKEN Nishina Center, Wako, Saitama 351-0198, Japan*

(Received 24 May 2021; accepted 15 November 2021; published 22 November 2021)

Background: The density profile of exotic nuclei can be a rich source of information on the nuclear surface. In particular, the nuclear surface diffuseness is correlated with the occupation probability of nucleons in distinct nuclear orbits, especially those with low angular momenta.
Purpose: The aim of this paper is to investigate the relationship between the nuclear surface diffuseness and spectroscopic information of neutron-rich Ne and Mg isotopes both at the cusp and inside the island of inversion.
Method: We use the microscopic antisymmetrized molecular dynamics model to calculate the densities and other spectroscopic information related to Ne and Mg isotopes. A two-parameter Fermi density distribution is then used to define the diffuseness parameter and the matter radius. These quantities are extracted by minimizing the difference between these two densities. To relate them with observables, the two densities are given as inputs to a Glauber model calculation of nucleon-nucleus elastic scattering differential cross section, with the demand that they reproduce the first peak position and its magnitude.
Results: A marked increase in the occupation of neutrons in the pf orbit is noted in Ne and Mg isotopes from $N = 19$ onwards. We observed that the nuclear surface diffuseness is strongly correlated with the nuclear deformation, in the island of inversion, and gradually increases with the occupation of neutrons in the $1p_{3/2}$ orbit. This result is also confirmed by a single-particle estimate of the valence neutron density distribution, with ^{29}Ne as a test case. An exception is noted for $^{35-37}$Mg, where the filling up of the holes in the sd shell partially compensates the increase in diffuseness due to filling up of the $1p_{3/2}$ orbit.
Conclusion: Information on nuclear density profile of neutron-rich medium mass nuclei can be reliably extracted by studying the first diffraction peak of the nucleon-nucleus elastic scattering differential cross section. The enormous surface diffuseness of Ne and Mg isotopes, in the island of inversion, could be attributed to the increasing neutron occupation of the $1p_{3/2}$ orbit.

DOI: 10.1103/PhysRevC.104.054313

I. INTRODUCTION

In recent times, investigations of the nuclear surface have revealed marked distinctions between exotic nuclei and their stable counterparts. For example, halos [1–3] and skins [4] have been seen in nuclei far from the valley of stability. The density profile of such exotic nuclei have been an abundant source of information on the nuclear surface. Recently, indication of the core swelling phenomenon was observed for neutron-rich Ca isotopes, suggesting that it crucially affects the density profile near the nuclear surface [5,6]. Another exotic phenomenon, a central depression of nuclear density profile, was reported [7,8]. The vacancy in the s orbit plays an essential role in bubble formation, resulting in a depletion of the central part of the nuclear density profile. Recently, the present authors reported that nuclei with bubble-like structure could have small nuclear surface diffuseness [9]. The nuclear surface diffuseness is closely related to the occupation probability near the Fermi level and increases when the nucleons occupy the low orbital angular momentum state. This suggests that nuclear surface diffuseness is very sensitive to the occupation of the nucleons in the distinct nuclear orbits and therefore a systematic investigation of the nuclear surface diffuseness is worth pursuing.

It has been known in the literature that in the medium mass region there exists a so-called island of inversion [10], where intruder configurations with particle-hole excitations across $N = 20$ shell gap in their ground state result in large deformation. Consequently, deviations from standard shell model estimates are expected in this region. The exotic structure is strongly correlated with shell evolution and deformation in the island of inversion. The nuclear deformations of Ne and Mg isotopes using the fully microscopic antisymmetrized molecular dynamics (AMD) with the Gogny-D1S interaction have been analyzed in Refs. [11–14]. The ground state properties (total binding energy, spin parity, and one neutron separation energy) and matter radii of the Ne and Mg isotopes are well reproduced by the AMD calculation. They reported a sudden rise in the quadrupole deformation, β_2, as the Nilsson orbitals

*vchoudhary@ph.iitr.ac.in
†whoriuchi@nucl.sci.hokudai.ac.jp
‡masaaki@nucl.sci.hokudai.ac.jp
§rchatterjee@ph.iitr.ac.in

originating from the spherical $0f_{7/2}$ shell gets filled for both the Ne and Mg isotopes, for $N = 19$–28. Given that deformation would change the nuclear density profile at or near the nuclear surface, the nuclear radius would also see a correlated increase. This was confirmed experimentally in systematic studies of the total reaction or interaction cross sections of Ne and Mg isotopes on a carbon target in Refs. [15–18]. We remark that in addition to the AMD approach with the Gogny-D1S interaction [11–14], Refs. [19,20] investigated the nuclear radii by using Skyrme-type effective interactions and showed that large quadrupole deformation is essential to describe those nuclei.

The extraction of the nuclear density profile is indeed a challenging issue. Traditionally, electron scattering has been used to measure the proton density profile [21] but it is difficult to extract the neutron density distribution even for stable nuclei [22]. In this context, proton-nucleus scattering has been applied successfully [23] to deduce the matter density distribution. Reference [24] discussed the high-energy nucleon-nucleus scattering as an effective tool to analyze the nuclear surface diffuseness. They showed that the information about the half-radius of the nuclear density profile is encoded in the first diffraction peak of the nucleon-nucleus elastic scattering differential cross section. Another extension of proton-nucleus scattering is to deduce the information about matter density distribution of unstable nuclei using inverse kinematics [25]. Therefore, this motivates us to investigate the relationship between the nuclear surface diffuseness and the spectroscopic information of nuclei, in the island of inversion, utilizing high-energy nucleon-nucleus scattering.

In this paper, we deduce the nuclear surface diffuseness of Ne and Mg isotopes in a systematic way. For this purpose, we use the two-parameter Fermi density (2pF) distribution, which defines the nuclear surface diffuseness [24]. The radius and diffuseness parameters in the 2pF distribution for neutron-rich Ne and Mg isotopes are determined so as to reproduce a realistic density distribution calculated with the antisymmetrized molecular dynamics (AMD). We then perform a systematic analysis to find the correlation between the nuclear surface diffuseness and various structure information of the neutron-rich Ne and Mg isotopes. Feasibility of extracting the diffuseness parameter using the proton-nucleus elastic scattering [24] is verified for this mass region by using the Glauber model.

This paper is organized in the following way. In Sec. II, we give the requisite details of the AMD model relevant for our calculations. We also briefly explain the formalism of nucleon-nucleus collision at high incident energy within the Glauber model, wherein the elastic scattering differential cross sections are evaluated. The results and discussions on the neutron-rich Ne and Mg isotopes appear in Sec. III, followed by the conclusions in Sec. IV.

II. THEORETICAL FORMALISM

A. Density and occupation numbers from antisymmetrized molecular dynamics

We use AMD as a nuclear structure model to calculate the density and occupation numbers of Ne and Mg isotopes. We start with an A-body Hamiltonian

$$H = \sum_{i=1}^{A} t_i - t_{\rm cm} + \sum_{i<j}^{A} v_{ij}, \tag{1}$$

where v_{ij} denotes the Gogny D1S density functional plus Coulomb interaction. The center-of-mass kinetic energy $t_{\rm cm}$ is subtracted without approximation.

The variational wave function is the parity-projected Slater determinant of nucleon wave packets

$$\Phi^{\pi} = P^{\pi}\mathcal{A}\{\varphi_1 \cdots \varphi_A\}, \tag{2}$$

where P^{π} denotes the parity ($\pi = \pm$) projector. The nucleon wave packets have a Gaussian form

$$\varphi_i = \prod_{\sigma=x,y,z} \exp\{-\nu_\sigma (r_\sigma - Z_{i\sigma})^2\} \times \left(a_i \chi_{\frac{1}{2},\frac{1}{2}} + b_i \chi_{\frac{1}{2},-\frac{1}{2}}\right)(|p\rangle \text{ or } |n\rangle). \tag{3}$$

The centroids $\boldsymbol{Z}_i$, width $\boldsymbol{\nu}$, and the spin direction a_i and b_i of the wave packets are variational parameters. They are determined by minimizing the following energy with β constraint term:

$$E(\beta) = \frac{\langle \Phi^{\pi}|H|\Phi^{\pi}\rangle}{\langle \Phi^{\pi}|\Phi^{\pi}\rangle} + v_\beta(\langle\beta\rangle - \beta)^2, \tag{4}$$

where the strength of the constraint v_β is chosen as sufficiently large value to obtain the optimized wave function $\Phi^{\pi}(\beta)$, which has the minimum energy for each given value of the deformation parameter β.

The optimized wave functions are projected to the eigenstate of the angular momentum and superposed to describe the ground state

$$\Psi_M^{J\pi} = \sum_{iK} g_{iK} P_{MK}^{J} \Phi^{\pi}(\beta_i), \tag{5}$$

where the deformation parameter β is employed as a generator coordinate. The coefficients g_{iK} and the ground state energy are obtained by solving the Hill-Wheeler equation [26].

The point nucleon densities are calculated from the ground state wave functions as

$$\rho_{JM}(\boldsymbol{r}) = \left\langle \Psi_M^{J\pi} \middle| \sum_i \delta^3(\boldsymbol{r}_i - \boldsymbol{r}_{\rm cm} - \boldsymbol{r}) \middle| \Psi_M^{J\pi} \right\rangle = \sum_l C_{JMl0}^{JM} \rho_J^l(r) Y_{l0}(\hat{r}), \tag{6}$$

where $\boldsymbol{r}_{\rm cm}$ denotes the center-of-mass coordinate. The $l = 0$ component of the density $\rho_J^l(r)$ has been used as an input for the Glauber calculation, although the odd-mass nuclei can have the nonspherical densities with $l \neq 0$.

The occupation numbers of the sd and pf shells are evaluated in the same manner with Refs. [9,27]. First, we choose the single Slater determinant $\Phi^{\pi}(\beta)$, which has the maximum overlap with the ground state wave function $|\langle P_{MK}^{J}\Phi^{\pi}(\beta)|\Psi_M^{J\pi}\rangle|^2$, and regard it as an approximate ground state. This approximation may be reasonable as the maximum value of the overlap were larger than 0.90 for all nuclei. Then, we calculate the neutron single-particle wave functions $\widetilde{\varphi}_i$ of

the approximate ground state wave function, and consider the multipole decomposition

$$\widetilde{\varphi}_i(\boldsymbol{r}) = \sum_{jlm} \widetilde{\varphi}_{i;jlm}(r)[Y_l(\hat{r}) \times \chi_{\frac{1}{2}}]_{jm}. \tag{7}$$

The norm of $\widetilde{\varphi}_{i;jlm}(r)$ gives us an estimate of the neutron occupation numbers. The number of the neutron particles in pf orbit is given as

$$m(p),\ m(f) = \sum_{ijm} \langle \widetilde{\varphi}_{i;jlm} | \widetilde{\varphi}_{i;jlm} \rangle - n_{\rm core}, \tag{8}$$

where $n_{\rm core}$ is taken as $n_{\rm core} = 6$ for the $1p$ ($l = 1$) orbit and 0 for the $0f$ ($l = 3$) orbit as we assume the complete filling of the $0p$ orbits by the inert core. In the same manner, the number of holes in the sd orbits relative to the $N = 20$ shell closure is given as

$$n(sd) = n_{\rm core} - \sum_{l=0,2} \sum_{ijm} \langle \widetilde{\varphi}_{i;jlm} | \widetilde{\varphi}_{i;jlm} \rangle\,, \tag{9}$$

where $n_{\rm core} = 14$ for the assumption of the complete filling of the $0s_{1/2}$ and $0d_{5/2}$ orbits.

B. Nucleon-nucleus reactions with Glauber model

A powerful description of high-energy nuclear reactions was introduced by Glauber [28]. In the collision of a nucleon-nucleus system within the eikonal and adiabatic approximations, the elastic scattering amplitude of the Glauber model including the nuclear ($e^{i\chi_N}$) and the elastic Coulomb ($e^{i\chi_C}$) phase-shift functions can be calculated by [29]

$$F(\boldsymbol{q}) = \frac{iK}{2\pi} \int d\boldsymbol{b}\, e^{-i\boldsymbol{q}\cdot\boldsymbol{b}} (1 - e^{i\chi_N(\boldsymbol{b}) + i\chi_C(\boldsymbol{b})}), \tag{10}$$

where $\boldsymbol{q}$ is the momentum transfer vector, K is incident relativistic wave number corresponding to the projectile-target relative motion, and $\boldsymbol{b}$ is the impact parameter vector. The elastic scattering amplitude can be further simplified as

$$F(\boldsymbol{q}) = e^{2i\eta \ln(2Kr_c)} \Bigg[F_c(\boldsymbol{q}) + \frac{iK}{2\pi} \int d\boldsymbol{b}\, e^{-i\boldsymbol{q}\cdot\boldsymbol{b} + 2i\eta \ln(b)} (1 - e^{i\chi_N(\boldsymbol{b})}) \Bigg], \tag{11}$$

where r_c is the distance beyond which the Coulomb potential is switched off, whereas incidentally the differential cross section does not depend on r_c, the Rutherford scattering amplitude

$$F_c(\boldsymbol{q}) = -\frac{2K\eta}{\boldsymbol{q}} e^{-2i\eta \ln(\sin(\theta/2)) + 2i\sigma_0}, \tag{12}$$

with θ as the center of mass scattering angle, η as the Sommerfeld parameter, and $\sigma_0 = \arg\Gamma(1 + i\eta)$. The elastic scattering differential cross section can then be calculated using

$$\frac{d\sigma}{d\Omega} = |F(\boldsymbol{q})|^2. \tag{13}$$

In general, the evaluation of the nuclear phase-shift function is demanding because it contains multiple integrations. However, we employ the optical-limit approximation (OLA) [28,29] for the sake of simplicity. In the OLA, the multiple scattering effects are ignored by taking only the leading-order term of the cumulant expansion of the original phase-shift function. In the case of proton-nucleus scattering, the OLA works well, as demonstrated in Refs. [24,30–34]. The optical phase-shift function for the nucleon-nucleus scattering in the OLA is given by

$$e^{i\chi_N(\boldsymbol{b})} \approx \exp\left[-\int d\boldsymbol{r} \rho_N(\boldsymbol{r}) \Gamma_{NN}(\boldsymbol{b} - \boldsymbol{s}) \right], \tag{14}$$

where $\boldsymbol{r} = (\boldsymbol{s}, z)$, and $\boldsymbol{s}$ is the two-dimensional vector orthogonal to the incident beam direction z. $\rho_N(\boldsymbol{r})$ denotes the density distributions of the target nucleus. The profile function Γ_{NN} for the nucleon-nucleon scattering is incident energy dependent and is usually parameterized as given in Ref. [35]:

$$\Gamma_{NN}(\boldsymbol{b}) = \frac{1 - i\alpha_{NN}}{4\pi\beta_{NN}} \sigma_{NN}^{\rm tot} \exp\left(-\frac{\boldsymbol{b}^2}{2\beta_{NN}} \right), \tag{15}$$

where α_{NN} is the ratio of the real part to the imaginary part of the nucleon-nucleon scattering amplitude in the forward direction, β_{NN} is the slope parameter of the differential cross section, and $\sigma_{NN}^{\rm tot}$ is the nucleon-nucleon total cross section. Standard parameter sets of the profile function are listed in Refs. [36,37].

C. Nuclear surface diffuseness

Let us now define the nuclear surface diffuseness used in this paper. We assume that the nuclear matter density profile with the mass number A being approximated by a two-parameter Fermi (2pF) distribution as

$$\rho_{2pF}(r) = \frac{\rho_0}{1 + \exp\left[(r - R)/a\right]}, \tag{16}$$

where R and a are the radius and diffuseness parameters, respectively. The ρ_0 value is uniquely determined for a given R and a by the normalization condition, $\int \rho(r) d\boldsymbol{r} = A$. Note that nuclear deformation induces in general more diffused nuclear surface compared to a spherical one [38] and most of the Ne and Mg isotopes considered here are deformed [13,14,19]. As prescribed in Ref. [24], the nuclear surface density profiles, even though they are deformed, can be described fairly well

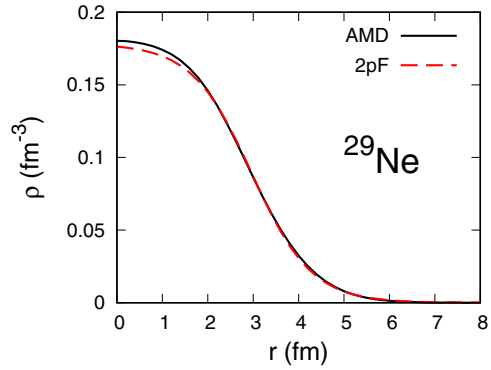

FIG. 1. Nuclear matter density distributions of ^{29}Ne by AMD and the one approximated by the 2pF function.

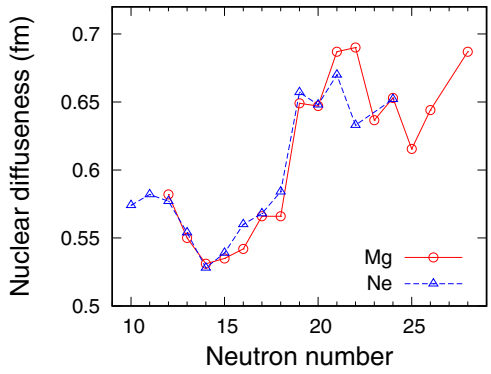

FIG. 2. Nuclear surface diffuseness of Ne and Mg isotopes as a function of neutron number.

by taking the R and a values so as to reproduce the first peak position and its magnitude of the elastic scattering differential cross section. Later we will verify that approach for the application to the neutron-rich Ne and Mg isotopes.

Meanwhile, we evaluate the diffuseness parameters directly from any structure model densities by minimizing the quantity as

$$\frac{4\pi}{A}\int_0^\infty |\rho(r)-\rho_{\rm 2pF}(r)|r^2dr, \tag{17}$$

where ρ is the point matter density distribution obtained with a structure model calculation. Figure 1 shows an example of the point matter density distribution of ^{29}Ne obtained with AMD, which exhibits large quadrupole deformation $\beta_2 = 0.445$ [13]. Though the 2pF distribution deviates in the internal region at $r \lesssim 2$ fm, it nicely describes the AMD density distributions around the nuclear surface from ≈2–4 fm. Hereafter we use the diffuseness parameters obtained directly from the AMD densities unless otherwise mentioned.

III. RESULTS AND DISCUSSIONS

A. Evolution of the nuclear surface diffuseness for Ne and Mg isotopes

Figure 2 plots the nuclear surface diffuseness of Ne and Mg isotopes extracted from the matter density distributions obtained by AMD. Reflecting the similarity in the nuclear deformations [13,14], the diffuseness parameter of Ne and Mg isotopes also show similar dependence on neutron number. We found that the neutron occupation of the weakly bound $1p_{3/2}$ orbit strongly influences the global behavior of the diffuseness parameter. To elucidate this point, Table I lists the number of neutrons in the pf orbits and holes in the sd orbits for nuclei with $N \geqslant 18$, and Fig. 3 illustrates the dominant particle-hole configuration of each nucleus estimated from Table I.

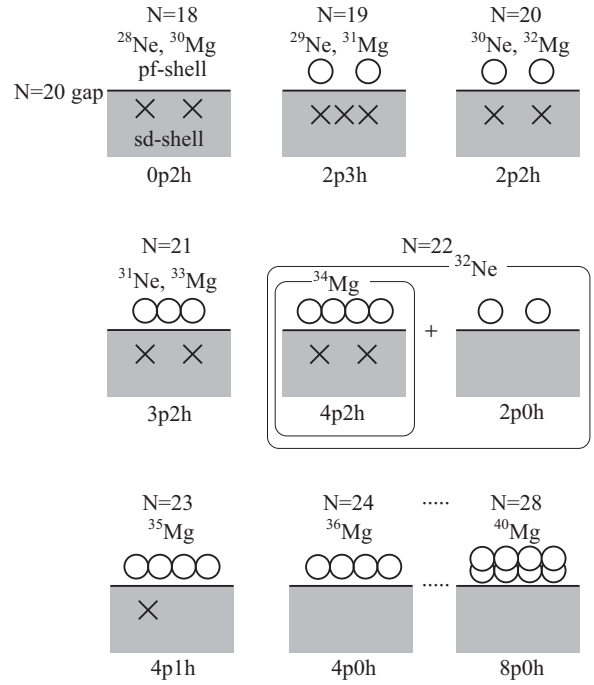

FIG. 3. Schematic illustrations of the $mpnh$ configurations relative to the $N = 20$ shell closure. The circles indicate the particles in pf shell while the crosses indicate the holes in sd shell.

The nuclei up to $N = 18$ have approximately zero particles in pf orbits, which is the normal filling expected from the ordinary shell structure. Consequently, their diffuseness parameters are close to the standard value of 0.54 fm [39].

TABLE I. Occupation numbers of Ne and Mg isotopes with $N \geqslant 18$. See text for details.

		Ne				Mg			
N	J^π	$m(p)$	$m(f)$	$m(pf)$	$n(sd)$	$m(p)$	$m(f)$	$m(pf)$	$n(sd)$
18	0^+	−0.03	0.08	0.05	2.12	0.24	0.27	0.50	2.66
19	$1/2^+$	0.82	1.16	1.98	3.26	0.76	1.18	1.94	3.36
20	0^+	0.84	1.14	1.97	2.26	0.76	1.21	1.97	2.27
21	$3/2^-$	0.97	1.93	2.91	2.28	0.92	1.95	2.87	2.39
22	0^+	0.97	1.72	2.69	1.07	1.12	2.70	3.81	2.39
23	$3/2^+$	–	–	–	–	1.01	2.86	3.87	1.26
24	0^+	1.02	2.90	3.91	0.22	0.98	2.94	3.92	0.24
25	$5/2^-$	–	–	–	–	1.07	3.82	4.89	0.24
26	0^+	–	–	–	–	1.40	4.46	5.87	0.30
28	0^+	–	–	–	–	1.97	5.78	7.75	0.35

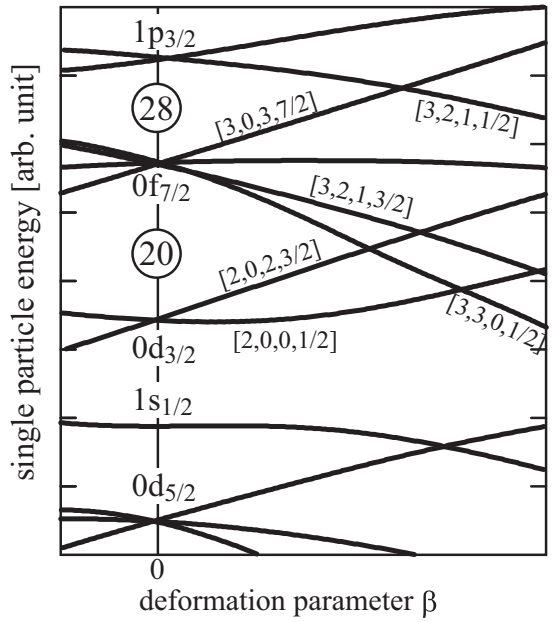

FIG. 4. A schematic Nilsson diagram for prolate deformation.

The particle-hole configuration is drastically changed in the island of inversion because of the loss of the magic number $N = 20$. The ground states of $N = 19$ nuclei, ^{29}Ne and ^{31}Mg, are dominated by a 2p3h configuration in which two neutrons are promoted into the pf orbits across the $N = 20$ shell gap. This intruder configuration induces strong quadrupole deformation and the mixing of the f and p waves. Consequently, these nuclei have sizable occupation numbers of the $1p_{3/2}$ orbit (0.82 in ^{29}Ne and 0.76 in ^{31}Mg) as well as $0f_{7/2}$. Note that the $1p_{3/2}$ orbit is located above the $N = 28$ shell gap in stable nuclei. Therefore, the occupation of the $1p_{3/2}$ orbit means that the magic numbers 20 and 28 are simultaneously lost in the island of inversion. Since the $1p_{3/2}$ orbit has large diffuseness, the density distributions of the $N = 19$ nuclei are also diffused compared to $N = 18$ nuclei. This situation may be more simply explained by the Nilsson orbits illustrated in Fig. 4. In the $N = 19$ nuclei, the two neutrons occupy an intruder orbit with the asymptotic quantum number $[N, N_z, \Lambda, \Omega] = [3, 3, 0, 1/2]$, which originates in the spherical $0f_{7/2}$ orbit. Because of the deformation and weak binding, this orbit is an admixture of the p and f waves. So, the intruder orbit $[3, 3, 0, 1/2]$ is the cause of large diffuseness of $N = 19$ nuclei.

The isotopes from $N = 19$ to $N = 21$ (^{31}Ne) and $N = 22$ (^{33}Mg) are also regarded as the nuclei in the island of inversion because their ground states are also dominated by the intruder mpnh configurations with $m, n > 0$. Similarly to the $N = 19$ nuclei, strong deformation mixes the f and p waves and increases the diffuseness. In terms of the Nilsson orbit, the intruder $[3, 3, 0, 1/2]$ and $[3, 2, 1, 3/2]$ orbits are playing a role for diminishing the $N = 20$ and 28 shell gaps and creating the island of inversion.

At ^{35}Mg ($N = 23$), the intruder orbits $[3, 3, 0, 1/2]$ and $[3, 2, 1, 3/2]$ are fully occupied, and the holes in the sd orbits start to be filled. Because the sd orbits are deeply bound, they partially cancel out the diffuseness increased by $1p_{3/2}$. As a result, the diffuseness parameter slightly reduces toward ^{37}Mg ($N = 25$). At $N = 24$, the holes in sd shell are completely filled, and hence one may regard ^{36}Mg as the border of the island of inversion.

In the $N = 26$ and 28 nuclei, another intruder orbit $[3, 2, 1, 1/2]$, which originates in the spherical $1p_{3/2}$ orbit comes down and is inverted with the orbit $[3, 0, 3, 7/2]$ leading to the explicit loss of the $N = 28$ magicity [27,40,41]. Since this intruder orbit is also an admixture of the p and f waves, the occupation number of $1p_{3/2}$ gradually increases resulting in the growth of the diffuseness toward ^{40}Mg. Thus, the global behavior of the diffuseness parameter can be explained by the occupation of $1p_{3/2}$.

Let us now comment on the structure and diffuseness parameters of these isotopes. First, we note that $N = 22$ nuclei ^{34}Mg and ^{32}Ne have slightly different diffuseness parameters in the present calculation. We found that ^{34}Mg is dominated by a 4p2h configuration, while ^{32}Ne is an admixture of a 4p2h and a 2p0h configurations. Hence, ^{34}Mg has larger diffuseness parameter than ^{32}Ne. Second, we note that the spin parity of ^{29}Ne, ^{35}Mg, and ^{37}Mg have not been firmly determined yet. For example, our calculation suggests the $1/2^+$ ground state of ^{29}Ne, while a shell model calculation suggests the $3/2^+$ ground state [42,43]. Contrary to these theoretical results, the $3/2^-$ ground state was suggested by a Coulomb breakup experiment [44]. As different spin parity means different particle-hole configurations, we expect that more detailed analysis of the diffuseness will identify the spin parity of these nuclei. However, to make our discussion transparent, we only adopted the spin parity calculated by AMD.

B. Single-particle model analysis for nuclear surface diffuseness

Based on the spectroscopic information obtained from the AMD wave function, here we attempt to understand the large diffuseness values for $N > 18$ through a single-particle model approach. Assuming that an $N = 18$ isotope is a core nucleus with 0p2h configuration, we consider multiparticle-multihole ($\bar{m}$p$\bar{n}$h) configurations for the valence neutrons according to the dominant configurations illustrated in Fig. 3. The normalized valence neutron orbits $\phi(nl_j)$ are generated by the following core-neutron potential [39]:

$$U = V_0 f(r) + V_1 r_0^2 \boldsymbol{l} \cdot \boldsymbol{s} \frac{1}{r} \frac{d}{dr} f(r). \tag{18}$$

The Woods-Saxon form factor $f(r) = \{1 + \exp[(r - R_c)/a_c]\}^{-1}$ is employed. We take $R_c = r_0 A_c^{1/3}$, where $r_0 = 1.25$ fm, $A_c = 28$ (30) for the Ne (Mg) isotopes with $N \geqslant 19$, and $a_c = 0.75$ fm. The spin-orbit strength is taken to follow the systematics [39] $V_1 = 18.0$ (19.2) MeV for the Ne (Mg) isotopes. This parameter set reasonably reproduced the level structure at around the island of inversion [45]. We generate the single-particle wave functions by varying V_0 and construct the nuclear density as

$$\rho = \rho_c(N_c = 18) + \rho_v(N_v), \tag{19}$$

TABLE II. Nuclear surface diffuseness, a, and rms point matter radii, r_m, of Ne and Mg isotopes extracted from the elastic scattering differential cross sections at various incident energies E in MeV. The values in parentheses are the results without the elastic Coulomb phase. The a values extracted directly by minimizing the difference between the AMD and 2pF density distributions (see Sec. III A) are listed as AMD for comparison. AMD* shows the rms point matter radii calculated with the original AMD density distributions.

	a (fm)				r_m (fm)				
nucleus	$E = 325$	550	800	AMD	$E = 325$	550	800	AMD	AMD*
^{20}Ne	0.579(0.582)	0.578(0.579)	0.571(0.570)	0.574	3.049(3.044)	3.039(3.040)	3.031(3.025)	2.984	2.925
^{21}Ne	0.586(0.590)	0.585(0.586)	0.577(0.577)	0.582	3.088(3.089)	3.078(3.079)	3.066(3.066)	3.023	2.962
^{22}Ne	0.579(0.582)	0.577(0.578)	0.570(0.570)	0.577	3.104(3.099)	3.088(3.090)	3.082(3.081)	3.043	2.983
^{23}Ne	0.552(0.554)	0.551(0.551)	0.544(0.544)	0.554	3.076(3.071)	3.071(3.067)	3.060(3.059)	3.030	2.977
^{24}Ne	0.520(0.522)	0.519(0.519)	0.514(0.514)	0.528	3.041(3.042)	3.039(3.036)	3.035(3.034)	3.013	2.967
^{25}Ne	0.533(0.536)	0.531(0.532)	0.524(0.524)	0.539	3.094(3.091)	3.083(3.085)	3.076(3.076)	3.049	2.996
^{26}Ne	0.558(0.563)	0.557(0.558)	0.547(0.547)	0.560	3.174(3.172)	3.164(3.164)	3.150(3.151)	3.123	3.049
^{27}Ne	0.566(0.571)	0.565(0.566)	0.555(0.555)	0.568	3.235(3.235)	3.226(3.226)	3.212(3.211)	3.184	3.114
^{28}Ne	0.582(0.586)	0.580(0.581)	0.570(0.570)	0.584	3.317(3.310)	3.302(3.302)	3.288(3.288)	3.265	3.191
^{29}Ne	0.658(0.663)	0.658(0.669)	0.647(0.647)	0.656	3.435(3.429)	3.424(3.423)	3.404(3.405)	3.352	3.282
^{30}Ne	0.662(0.669)	0.661(0.663)	0.648(0.648)	0.655	3.490(3.485)	3.470(3.473)	3.449(3.449)	3.410	3.315
^{31}Ne	0.684(0.692)	0.684(0.686)	0.670(0.670)	0.676	3.563(3.559)	3.547(3.549)	3.525(3.529)	3.475	3.374
^{32}Ne	0.633(0.638)	0.632(0.633)	0.621(0.621)	0.633	3.509(3.504)	3.499(3.498)	3.482(3.482)	3.450	3.370
^{34}Ne	0.646(0.652)	0.645(0.646)	0.634(0.635)	0.652	3.583(3.582)	3.572(3.571)	3.559(3.565)	3.526	3.438
^{24}Mg	0.581(0.585)	0.581(0.582)	0.574(0.574)	0.582	3.164(3.161)	3.158(3.158)	3.150(3.149)	3.109	3.049
^{25}Mg	0.547(0.550)	0.546(0.547)	0.540(0.541)	0.550	3.121(3.118)	3.112(3.113)	3.105(3.110)	3.073	3.028
^{26}Mg	0.522(0.524)	0.521(0.522)	0.515(0.515)	0.531	3.099(3.094)	3.093(3.095)	3.083(3.083)	3.072	3.018
^{27}Mg	0.530(0.534)	0.530(0.530)	0.524(0.524)	0.535	3.135(3.138)	3.134(3.129)	3.128(3.127)	3.095	3.051
^{28}Mg	0.533(0.537)	0.532(0.533)	0.526(0.526)	0.542	3.174(3.173)	3.165(3.165)	3.161(3.161)	3.130	3.082
^{29}Mg	0.565(0.571)	0.565(0.567)	0.556(0.556)	0.566	3.280(3.273)	3.265(3.270)	3.254(3.253)	3.233	3.166
^{30}Mg	0.560(0.565)	0.559(0.560)	0.550(0.550)	0.566	3.305(3.297)	3.290(3.289)	3.278(3.278)	3.258	3.191
^{31}Mg	0.646(0.653)	0.646(0.648)	0.637(0.637)	0.649	3.452(3.453)	3.439(3.442)	3.429(3.428)	3.387	3.315
^{32}Mg	0.647(0.655)	0.647(0.650)	0.637(0.637)	0.647	3.485(3.482)	3.466(3.474)	3.453(3.455)	3.419	3.336
^{33}Mg	0.688(0.697)	0.689(0.692)	0.677(0.677)	0.687	3.603(3.598)	3.585(3.592)	3.569(3.568)	3.519	3.428
^{34}Mg	0.691(0.701)	0.692(0.695)	0.679(0.680)	0.690	3.639(3.634)	3.620(3.625)	3.603(3.604)	3.550	3.450
^{35}Mg	0.636(0.644)	0.637(0.638)	0.626(0.627)	0.635	3.545(3.547)	3.539(3.536)	3.522(3.528)	3.482	3.408
^{36}Mg	0.648(0.654)	0.648(0.649)	0.638(0.638)	0.653	3.602(3.595)	3.591(3.588)	3.579(3.579)	3.542	3.466
^{37}Mg	0.608(0.614)	0.607(0.608)	0.600(0.600)	0.616	3.557(3.552)	3.544(3.543)	3.540(3.534)	3.510	3.441
^{38}Mg	0.636(0.642)	0.635(0.637)	0.628(0.628)	0.644	3.646(3.639)	3.632(3.636)	3.622(3.622)	3.590	3.511
^{40}Mg	0.680(0.688)	0.679(0.681)	0.666(0.666)	0.687	3.779(3.776)	3.763(3.765)	3.745(3.745)	3.711	3.620

where $\rho_c(N_c = 18)$ is the density distribution of ^{28}Ne or ^{30}Mg obtained by the AMD calculation, and $\rho_v(N_v)$ is the density distribution of the valence neutrons defined by

$$\rho_v = \bar{m}[\alpha|\phi(1p_{3/2})|^2 + (1-\alpha)|\phi(0f_{7/2})|^2)] - \bar{n}|\phi(0d_{3/2})|^2. \quad (20)$$

In this model, the number of the valence neutrons satisfies $N_v = \bar{m} - \bar{n}$. The $\bar{m}$ is the number of particle states that share the $1p_{3/2}$ and $0f_{7/2}$ orbits with mixing probability $\alpha = m(p)/m(pf)$ listed in Table I. The $|\bar{n}|$ describes the number of the hole ($\bar{n} > 0$) or particle state ($\bar{n} < 0$) measured from the core nucleus ($N = 18$). The particle or hole state in the sd shell is assumed to be $0d_{3/2}$. Here we take the most plausible configuration for each isotope, which corresponds to the $\bar{m}$p$(\bar{n}-2)$h configurations drawn in Fig. 3 according to the spectroscopic information of the AMD wave function. More specifically, we take $(\bar{m}, -\bar{n}) = (2,-1)$, (2,0), (3,0), (3,1), and (4,2) for $^{29-32,34}$Ne, and $(\bar{m}, -\bar{n}) = (2,-1)$, (2,0), (3,0), (4,0), (4,1), (4,2), (5,2), (6,2), and (8,2) for $^{31-38,40}$Mg, respectively. Finally, the potential strength V_0 is fixed for each isotope so as to reproduce the root-mean-square (rms) matter radius obtained by the AMD (they are tabulated in Table II). This is reasonable because the behavior of the single-particle wave function near the nuclear surface crucially depends on its binding energy and will reflect in the nuclear radius. This effect can be incorporated in this model through the adjustment of V_0.

Using those calculated density distributions of the Ne and Mg isotopes for $N \geqslant 19$, we extract the diffuseness parameters directly from the model density by using Eq. (17). Figure 5 draws these extracted diffuseness parameters for $N \geqslant 19$. We find overall underestimation of the absolute value. This is partly because the AMD wave function is expressed by Gaussian wave packets and thus the density distribution at nuclear surface changes more sensitive to the occupation numbers. On the other hand, the isotope dependence is fairly well described: a sudden increase from $N = 18$–19 and showing a zigzag pattern for N increases further. Basically, the diffuseness parameter grows as an increase of the number of the particle in the pf shell and the hole of the sd shell. We will now discuss this feature in detail.

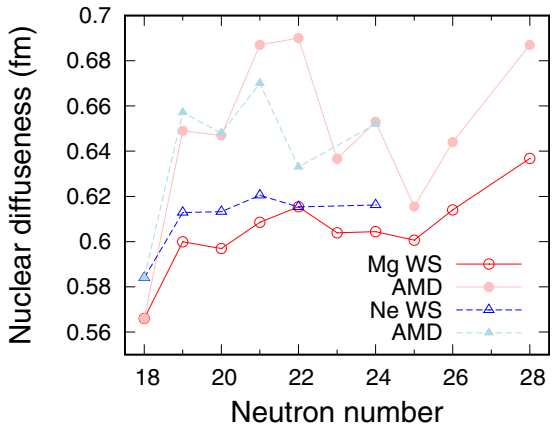

FIG. 5. Nuclear diffuseness parameters extracted from density distributions obtained by the single-particle model for $N > 18$. The AMD results (Fig. 2) are also plotted for comparison.

Figure 6 plots the density distributions of the valence neutrons ρ_v of ^{29}Ne obtained by the single-particle model analysis. We also plot the decompositions of the valence neutron density into the particle $1p_{3/2}$, $0f_{7/2}$ and hole $0d_{3/2}$ components, which correspond to the first to third terms in Eq. (20), respectively. The diffuseness parameter describes a slope around the radius parameter [46] and is also plotted as a vertical line at 3.13 fm. As expected, the single-particle density with the $1p_{3/2}$ orbit exhibits the most extended distribution just beyond the nuclear radius. The peak positions of the $0f_{7/2}$ particle and $0d_{3/2}$ hole states are different. The $0f_{7/2}$ particle state contributes the increase of the density around the nuclear radius, while the $0d_{3/2}$ hole plays to reduce the density below the nuclear radius. Summing up all those contributions, as a net, the valence neutron density reduces (increases) the density below (beyond) the nuclear radius, leading to the large diffuseness of the nuclear surface at $N = 19$ compared to $N = 18$. This is consistent with the finding of Ref. [47], in which contributions of the single-particle orbits to the nuclear

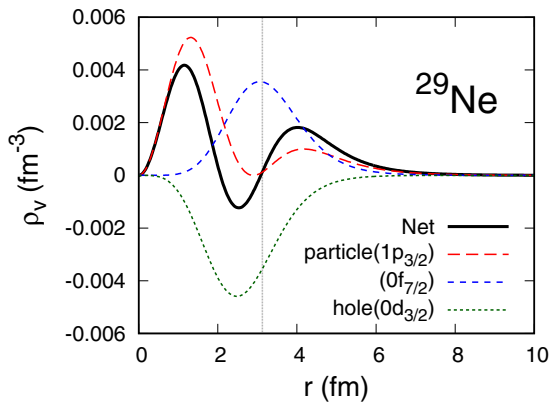

FIG. 6. Valence neutron density distribution and its decomposition into particle $1p_{3/2}$ and $0f_{7/2}$ states and $0d_{3/2}$ hole state. See text for details. A vertical thin dotted line denotes the radius parameter value 3.13, extracted from the density distribution obtained by the single-particle model.

surface diffuseness were discussed in detail. We also tried to make the same analysis by assuming the particle $0d_{3/2}$ configuration for the valence neutron following the spherical shell model filling. No bound $0d_{3/2}$ orbit was obtained to satisfy the condition of this single-particle model, and thus this assumption appears to be unrealistic.

At $N = 20$, the diffuseness parameter is reduced from $N = 19$ because the hole $0d_{3/2}$ state is filled by addition of a neutron. It again increases at $N = 21$ due to the occupation of a neutron in the pf shell. At $N = 22$, where the configurations of ^{32}Ne and ^{34}Mg are different. The diffuseness of ^{32}Ne decreases compared to ^{31}Ne due to the occupation of the particle $0d_{3/2}$ state, whereas for ^{34}Mg it increases due to the pf shell filling. For $N > 22$, since the sd shell is fully occupied, the diffuseness parameter gradually increases towards $N = 28$, showing a small kink at $N = 25$.

Though the present single-particle model analysis is somewhat qualitative, the evolution of the nuclear surface diffuseness tells us a variety of the structure information. A systematic determination of the nuclear surface diffuseness is interesting as it includes the spectroscopic information, which is essential in describing the exotic nuclear states in the island of inversion.

C. Extraction of the nuclear surface diffuseness from the reaction observables

Here we extract the nuclear surface diffuseness from the elastic scattering differential cross sections for the Ne and Mg isotopes. The unknown radius and diffuseness parameters are evaluated by using the elastic scattering differential cross section of a nucleus-proton reaction calculated with the Glauber model following the prescription given in Ref. [24]. First we compute the elastic scattering differential cross sections using realistic density distributions calculated with AMD. We then demand the R and a values of the 2pF distribution reproducing both the first peak position and its magnitude of the elastic scattering cross sections.

Table II lists the resulting a values obtained at various incident energies. We use a set of the parameters of the profile function in Ref. [36] and choose the incident energies of 325, 550, and 800 MeV, where the isospin dependence of the nucleon-nucleon cross section is neglected [24]. As was shown in Ref. [24], the extracted a values do not depend much on the incident energy. We also did the same analysis without the elastic Coulomb contribution. The results are listed in parentheses in Table II, and indicate that the elastic Coulomb contributions are negligible, as expected.

To verify this approach for the neutron-rich Ne and Mg isotopes, we compare the diffuseness parameters obtained directly from the AMD densities (see Sec. III A). As shown in Table II, the resulting diffuseness parameters indicated by "AMD" also agree with those obtained by the elastic scattering diffraction. The nuclear surface diffuseness of the neutron-rich Ne and Mg isotopes can be extracted as a robust quantity by measuring the nucleus-nucleon elastic scattering differential cross sections at the first peak position.

Table II also lists the rms point matter radii simultaneously obtained by the analysis of the elastic scattering cross section.

We also see good agreement between the results extracted from this analysis and the AMD results. However, it should be noted that the rms matter radius of the 2pF distribution tends to overestimate that of the original AMD density distributions (shown as AMD* in Table II) at most by ≈0.1 fm or typically in ≈3%. Since the tail of the AMD density drops as a Gaussian, the 2pF model density is not very appropriate to describe the tail regions of the AMD density, which contributes the rms radius. Actually, in the analysis of the single-particle model using the correct asymptotic tail, the deviation of the rms matter radii between the original and 2pF density distributions is reduced typically in ≈1%. In principle, both values can be determined more accurately by the 2pF distribution obtained from the first peak position and its magnitude of the elastic scattering differential scattering cross section as the rms radius and diffuseness are nicely reproduced when the density distributions of the Hartree-Fock method on grid points within ≈1% [24]. In a practical experimental situation, where only the peak position and its magnitude of the elastic scattering cross section is known, the matter radius and diffuseness can be determined by the 2pF model density within a certain accuracy.

IV. CONCLUSIONS

The island of inversion, in the medium mass region of the nuclear chart, is characterized by intruder configurations in the ground state of nuclei. Apart from resulting in large deformations the change in occupation of nucleons in different energy levels will impact the nuclear density profile, and in particular the nuclear surface diffuseness. In this work, we have discussed the relationship between the nuclear surface diffuseness and the spectroscopic information of nuclei at or close to the island of inversion, specifically for Ne and Mg isotopes with $N = 19$–28.

We have calculated the structure of Ne and Mg isotopes using the antisymmetrized molecular dynamics (AMD). We then construct a phenomenological two-parameter Fermi (2pF) density distribution, which has adjustable radius and diffuseness parameters. These parameters are then estimated by minimizing the difference in densities obtained by AMD and the 2pF density distribution. In a complementary approach the radius and diffuseness parameters, of the 2pF density distribution, are also determined so as to reproduce the first peak position and its magnitude of elastic scattering differential cross section obtained with the AMD densities in the Glauber model. The results obtained with these two approaches mostly agree within a limit of 1%–3%.

The AMD results reveal that there is a drastic increase in the occupation number of neutrons in the pf orbit from $N = 19$ onwards, compared to $N = 18$, in Ne and Mg isotopes. This intruder configuration induces a strong deformation owing to the mixing of the p and f orbits and signals the onset of the island of inversion in this mass range. We observed that the occupancy of the neutron in weakly bound $1p_{3/2}$ orbit has a significant impact on the overall behavior of the nuclear surface diffuseness. Given that the $1p_{3/2}$ orbit has a large diffuseness, nuclei with a sizable neutron occupation number in this orbit is also characterized by a large nuclear surface diffuseness. An estimate of the valence neutron density distribution using a single-particle model, with ^{29}Ne as a test case, also confirms this conclusion.

The breakdown of the $N = 20$ magic number changes the particle-hole configuration notably in the island of inversion. The 2p3h configuration, is dominant in the ground state of $N = 19$ nuclei, in which two neutrons occupy the pf orbits above the $N = 20$ shell gap. A similar behavior also observed for the loss of $N = 28$ (^{40}Mg) magic number due to increasing admixture of the p- and f-intruder orbits resulting in the increase of diffuseness in $^{38–40}$Mg. However, in $^{35–37}$Mg the filling up of the holes in the sd shell for $N = 23$–25 results in the relative reduction of the diffuseness.

We have also shown that the information on nuclear surface diffuseness of neutron-rich Ne and Mg isotopes can be obtained by calculating the first diffraction peak of nucleon-nucleus elastic scattering differential cross section. As expected, at high energies, the Coulomb contribution, in determining the surface diffuseness and matter radii of these isotopes is very small, typically less than 1%.

Finally, let us remark that a large surface diffuseness in neutron-rich Ne and Mg could have consequences in determining the abundance of these nuclei in explosive nucleosynthesis. In fact, properly accounting for the structure of these exotic medium mass isotopes is a prerequisite in subsequently determining the r-process path in neutron star mergers and in the postcollapse phase of a type II or type Ib supernova [48,49].

ACKNOWLEDGMENTS

This work was in part supported by JSPS KAKENHI Grants No. 18K03635 and No. 19K03859, the collaborative research programs 2021, Information Initiative Center, Hokkaido University and the Scheme for Promotion of Academic and Research Collaboration (SPARC/2018-2019/P309/SL), MHRD, India. V.C. also acknowledges MHRD, India for support via a doctoral fellowship and a grant from SPARC to visit the Hokkaido University.

[1] I. Tanihata, H. Hamagaki, O. Hashimoto, Y. Shida, N. Yoshikawa, K. Sugimoto, O. Yamakawa, T. Kobayashi, and N. Takahashi, Phys. Rev. Lett. **55**, 2676 (1985).

[2] I. Tanihata, H. Savajols, and R. Kanungo, Prog. Part. Nucl. Phys. **68**, 215 (2013), and references therein.

[3] S. Bagchi, R. Kanungo, Y. K. Tanaka, H. Geissel, P. Doornenbal, W. Horiuchi, G. Hagen, T. Suzuki, N. Tsunoda, D. S. Ahn, H. Baba, K. Behr, F. Browne, S. Chen, M. L. Cortes, A. Estrade, N. Fukuda, M. Holl, K. Itahashi, N. Iwasa, G. R. Jansen, W. G. Jiang, S. Kaur, A. O. Macchiavelli,

S. Y. Matsumoto, S. Momiyama, I. Murray, T. Nakamura, S. J. Novario, H. J. Ong, T. Otsuka, T. Papenbrock, S. Paschalis, A. Prochazka, C. Scheidenberger, P. Schrock, Y. Shimizu, D. Steppenbeck, H. Sakurai, D. Suzuki, H. Suzuki, M. Takechi, H. Takeda, S. Takeuchi, R. Taniuchi, K. Wimmer, and K. Yoshida, Phys. Rev. Lett. **124**, 222504 (2020).

[4] T. Suzuki, H. Geissel, O. Bochkarev, L. Chulkov, M. Golovkov, D. Hirata, H. Irnich, Z. Janas, H. Keller, T. Kobayashi, G. Kraus, G. Münzenberg, S. Neumaier, F. Nickel, A. Ozawa, A. Piechaczeck, E. Roeckl, W. Schwab, K. Sümmerer, K. Yoshida, and I. Tanihata, Phys. Rev. Lett. **75**, 3241 (1995).

[5] M. Tanaka, M. Takechi, M. Fukuda, D. Nishimura, T. Suzuki, Y. Tanaka, T. Moriguchi, D. S. Ahn, A. Aimaganbetov, M. Amano *et al.*, Phys. Rev. Lett. **124**, 102501 (2020).

[6] W. Horiuchi and T. Inakura, Phys. Rev. C **101**, 061301(R) (2020).

[7] M. Grasso, L. Gaudefroy, E. Khan, T. Nikšić, J. Piekarewicz, O. Sorlin, N. Van Giai, and D. Vretenar, Phys. Rev. C **79**, 034318 (2009).

[8] J. J. Li, W. H. Long, J. L. Song, and Q. Zhao, Phys. Rev. C **93**, 054312 (2016).

[9] V. Choudhary, W. Horiuchi, M. Kimura, and R. Chatterjee, Phys. Rev. C **102**, 034619 (2020).

[10] E. K. Warburton, J. A. Becker, and B. A. Brown, Phys. Rev. C **41**, 1147 (1990).

[11] K. Minomo, T. Sumi, M. Kimura, K. Ogata, Y. R. Shimizu, and M. Yahiro, Phys. Rev. C **84**, 034602 (2011).

[12] K. Minomo, T. Sumi, M. Kimura, K. Ogata, Y. R. Shimizu, and M. Yahiro, Phys. Rev. Lett. **108**, 052503 (2012).

[13] T. Sumi, K. Minomo, S. Tagami, M. Kimura, T. Matsumoto, K. Ogata, Y. R. Shimizu, and M. Yahiro, Phys. Rev. C **85**, 064613 (2012).

[14] S. Watanabe, K. Minomo, M. Shimada, S. Tagami, M. Kimura, M. Takechi, M. Fukuda, D. Nishimura, T. Suzuki, T. Matsumoto, Y. R. Shimizu, and M. Yahiro, Phys. Rev. C **89**, 044610 (2014).

[15] M. Takechi, T. Ohtsubo, T. Kuboki, M. Fukuda, D. Nishimura, T. Suzuki, T. Yamaguchi, A. Ozawa, T. Moriguchi, T. Sumikawa *et al.*, Mod. Phys. Lett. A **25**, 1878 (2010).

[16] M. Takechi, T. Ohtsubo, T. Kuboki, M. Fukuda, D. Nishimura, T. Suzuki, T. Yamaguchi, A. Ozawa, T. Moriguchi, T. Sumikawa *et al.*, Nucl. Phys. A **834**, 412c (2010).

[17] M. Takechi, T. Ohtsubo, M. Fukuda, D. Nishimura, T. Kuboki, T. Suzuki, T. Yamaguchi, A. Ozawa, T. Moriguchi, H. Ooishi *et al.*, Phys. Lett. B **707**, 357 (2013).

[18] M. Takechi, S. Suzuki, D. Nishimura, M. Fukuda, T. Ohtsubo, M. Nagashima, T. Suzuki, T. Yamaguchi, A. Ozawa, T. Moriguchi *et al.*, Phys. Rev. C **90**, 061305(R) (2014).

[19] W. Horiuchi, T. Inakura, T. Nakatsukasa, and Y. Suzuki, Phys. Rev. C **86**, 024614 (2012).

[20] W. Horiuchi, T. Inakura, T. Nakatsukasa, and Y. Suzuki, JPS Conf. Proc. **6**, 030079 (2015).

[21] H. de Vries, C. W. de Jager, and C. de Vries, At. Data Nucl. Data Tables **36**, 495 (1987).

[22] PREX Collaboration, S. Abrahamyan *et al.*, Phys. Rev. Lett. **108**, 112502 (2012).

[23] H. Sakaguchi and J. Zenihiro, Prog. Part. Nucl. Phys. **97**, 1 (2017), and references therein.

[24] S. Hatakeyama, W. Horiuchi, and A. Kohama, Phys. Rev. C **97**, 054607 (2018).

[25] Y. Matsuda, H. Sakaguchi, H. Takeda, S. Terashima, J. Zenihiro, T. Kobayashi, T. Murakami, Y. Iwao, T. Ichihara, T. Suda, T. Ohnishi, Y. Watanabe, H. Otsu, K. Yoneda, Y. Satou, K. Ozeki, and M. Kanazawa, Phys. Rev. C **87**, 034614 (2013).

[26] D. L. Hill and J. A. Wheeler, Phys. Rev. **89**, 1102 (1953).

[27] Y. Suzuki and M. Kimura, Phys. Rev. C **104**, 024327 (2021).

[28] R. J. Glauber, in *Lectures in Theoretical Physics*, edited by W. E. Brittin and L. G. Dunham (Interscience, New York, 1959), Vol. 1, p. 315.

[29] Y. Suzuki, R. G. Lovas, K. Yabana, and K. Varga, *Structure and Reactions of Light Exotic Nuclei* (Taylor & Francis, London, 2003).

[30] K. Varga, S. C. Pieper, Y. Suzuki, and R. B. Wiringa, Phys. Rev. C **66**, 034611 (2002).

[31] T. Nagahisa and W. Horiuchi, Phys. Rev. C **97**, 054614 (2018).

[32] B. Abu-Ibrahim, S. Iwasaki, W. Horiuchi, A. Kohama, and Y. Suzuki, J. Phys. Soc. Jpn. **78**, 044201 (2009).

[33] S. Hatakeyama, S. Ebata, W. Horiuchi, and M. Kimura, J. Phys.: Conf. Ser. **569**, 012050 (2014).

[34] S. Hatakeyama, S. Ebata, W. Horiuchi, and M. Kimura, JPS Conf. Proc. **6**, 030096 (2015).

[35] L. Ray, Phys. Rev. C **20**, 1857 (1979).

[36] W. Horiuchi, Y. Suzuki, B. Abu-Ibrahim, and A. Kohama, Phys. Rev. C **75**, 044607 (2007).

[37] B. Abu-Ibrahim, W. Horiuchi, A. Kohama, and Y. Suzuki, Phys. Rev. C **77**, 034607 (2008); **80**, 029903(E) (2009); **81**, 019901(E) (2010).

[38] W. Horiuchi and T. Inakura, Prog. Theor. Exp. Phys. **2021**, 103D02 (2021).

[39] A. Bohr and B. R. Mottelson, *Nuclear Structure*, Vol. I (W. A. Benjamin, New York, 1975).

[40] I. Hamamoto, Phys. Rev. C **79**, 014307 (2009).

[41] I. Hamamoto, Phys. Rev. C **93**, 054328 (2016).

[42] V. Tripathi, S. L. Tabor, P. F. Mantica, C. R. Hoffman, M. Wiedeking, A. D. Davies, S. N. Liddick, W. F. Mueller, T. Otsuka, A. Stolz, B. E. Tomlin, Y. Utsuno, and A. Volya, Phys. Rev. Lett. **94**, 162501 (2005).

[43] V. Tripathi, S. L. Tabor, C. R. Hoffman, M. Wiedeking, A. Volya, P. F. Mantica, A. D. Davies, S. N. Liddick, W. F. Mueller, A. Stolz, B. E. Tomlin, T. Otsuka, and Y. Utsuno, Phys. Rev. C **73**, 054303 (2006).

[44] N. Kobayashi, T. Nakamura, Y. Kondo, J. A. Tostevin, Y. Utsuno, N. Aoi, H. Baba, R. Barthelemy, M. A. Famiano, N. Fukuda, N. Inabe, M. Ishihara, R. Kanungo, S. Kim, T. Kubo, G. S. Lee, H. S. Lee, M. Matsushita, T. Motobayashi, T. Ohnishi, N. A. Orr, H. Otsu, T. Otsuka, T. Sako, H. Sakurai, Y. Satou, T. Sumikama, H. Takeda, S. Takeuchi, R. Tanaka, Y. Togano, and K. Yoneda, Phys. Rev. Lett. **112**, 242501 (2014).

[45] W. Horiuchi, Y. Suzuki, P. Capel, and D. Baye, Phys. Rev. C **81**, 024606 (2010).

[46] A. Kohama, K. Iida, and K. Oyamatsu, J. Phys. Soc. Jpn. **85**, 094201 (2016).

[47] W. Horiuchi, Prog. Theor. Exp. Phys. (2021), doi: 10.1093/ptep/ptab136.

[48] M. Terasawa, K. Sumiyoshi, T. Kajino, G. J. Mathews, and I. Tanihata, Astrophys. J. **562**, 470 (2001).

[49] Shubhchintak, R. Chatterjee, and R. Shyam, Phys. Rev. C **96**, 025804 (2017).